Mesoscale Energy Balance and Air–Sea Interaction in the Kuroshio Extension: Low-Frequency versus High-Frequency Variability

HAIYUAN YANG,[a,b] LIXIN WU,[a,b] PING CHANG,[c,d,e] BO QIU,[f] ZHAO JING,[a,b] QIUYING ZHANG,[c,d,e] AND ZHAOHUI CHEN[a,b]

[a] *Physical Oceanography Laboratory/Institute for Advanced Ocean Study, Ocean University of China, Qingdao, China*
[b] *Pilot National Laboratory for Marine Science and Technology (Qingdao), Qingdao, China*
[c] *Department of Oceanography, Texas A&M University, College Station, Texas*
[d] *Department of Atmospheric Sciences, Texas A&M University, College Station, Texas*
[e] *International Laboratory for High-Resolution Earth System Prediction, Texas A&M University, College Station, Texas*
[f] *Department of Oceanography, University of Hawai'i at Mānoa, Honolulu, Hawaii*

ABSTRACT: Using eddy-resolving Community Earth System Model (CESM) simulations, this study investigates mesoscale energetics and air–sea interaction at two different time-scale windows in the Kuroshio Extension (KE) region. Based on an energy budget analysis, it is found that both baroclinic and barotropic pathways contribute to eddy energy generation within the low-frequency window (longer than 3 weeks) in this region, while both air–sea heat fluxes and wind stresses act as prominent eddy killers that remove energy from the ocean. In contrast, within the high-frequency window oceanic variability is mainly fed by baroclinic instability and regulated by turbulent thermal wind (TTW) processes, while the positive wind work is derived primarily from ageostrophic flow, i.e., Ekman drift, and along with air–sea heat fluxes has little influence on geostrophic mesoscale eddies.

KEYWORDS: Atmosphere-ocean interaction; Mesoscale processes; Ocean dynamics; Microscale processes/variability; Energy budget/balance; Oceanic variability

1. Introduction

The Kuroshio Extension (KE) is the western boundary current extension of the subtropical gyre in the North Pacific Ocean and, it is formed after the Kuroshio separates from the coast of Japan. Being an intense baroclinic inertial jet, the KE is characterized by the presence of two quasi-stationary meanders and energetic pinched-off eddies (Fig. 1a) (e.g., Qiu et al. 1991; Nakano et al. 2013; Kida et al. 2015; Sasaki and Minobe 2015). Based on long-term satellite altimeter measurements and high-resolution ocean model simulations, significant advancements have been made over the last two decades regarding the phenomenology and dynamic causes for mesoscale variability of KE. A rich literature is now available, suggesting that the mesoscale eddies draw their energy from mean flow mainly through both baroclinic (BC) and barotropic (BT) instability in the upstream KE, whereas they are dissipated or give energy back to mean flow in the downstream (Berloff and McWilliams 1999; Waterman and Jayne 2011; Yang and Liang 2016; Yang et al. 2018).

Regulated by westward-propagating baroclinic long Rossby waves and jet stability, the KE exhibits significant decadal modulations between a stable and an unstable dynamic state (Qiu and Chen 2005, 2010; Taguchi et al. 2007; Qiu et al. 2017; Yang et al. 2017, 2018). When in its stable dynamic state, the KE has been observed to have an intensified eastward transport, a northward latitudinal position, an enhanced southern recirculation gyre, and a decreased regional eddy kinetic energy (EKE) level. The reverse is true when the KE switches to an unstable dynamic state. The mesoscale variability in the KE region has been recognized to be important for the basin-scale ocean dynamics and marine ecosystems in the North Pacific (Qiu and Chen 2011; Bishop 2013; Kida et al. 2015).

In addition to its oceanic variability, the KE is also well known for its intense air–sea interaction. Carried by the strong Kuroshio Current, the warm water from the tropics is transported northward and exposed to the colder and windier atmosphere, resulting in large loss of heat from the ocean to the atmosphere (Fig. 1b). Particularly, the heating effect of the KE on the overlying atmosphere can reach more than $600 \, \mathrm{W \, m^{-2}}$ during boreal winter (Konda et al. 2010; Kelly et al. 2010). The heat and moisture provided by the underlying ocean regulate the instability of air and play an important role in the formation of storm tracks (Nakamura et al. 2004; Sampe and Xie 2007; Booth et al. 2010; Liu et al. 2018). In addition to the thermodynamic interaction, wind stress in this region is significantly influenced by strong ocean currents (Cornillon and Park 2001; Kelly et al. 2001; Renault et al. 2016). It has been hypothesized that the KE jet, wind stress, and atmospheric storms can form a coupled system at decadal time scales: wind-generated, westward-propagating baroclinic Rossby waves from the central North Pacific basin regulate the KE jet, while the dynamic state of the KE influences the storm tracks and surface wind stress curl field in return (Qiu et al. 2014).

Besides large-scale characteristics, the air–sea interaction in the KE region features prominent mesoscale variability as well. By examining the relationship between wind stress curl and crosswind component of local sea surface temperature (SST) gradient, Chelton et al. (2004) detected a dynamical
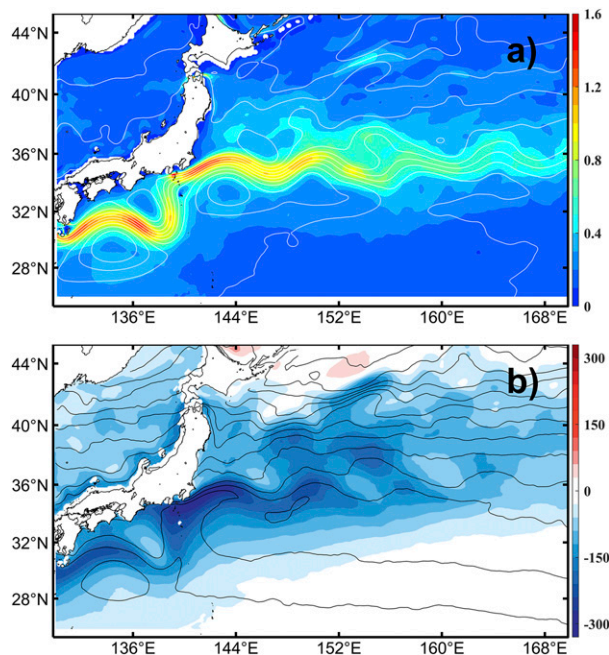
FIG. 1. (a) Mean velocity field (colored shading; m s^{-1}) based on the CESM in the western North Pacific. Contours denote the mean SSH field. (b) Mean surface downward net heat flux (colored shading; W m^{-2}) based on the CESM in the western North Pacific. Contours denote the mean SST field.

coupling between eddies and atmosphere. Based on the theoretical analysis using an eddy-centric framework, Gaube et al. (2015) investigated the effect of eddy current feedback induced by several factors. Current-induced surface wind stress curl change over an eddy can generate an Ekman pumping velocity that is of the opposite sign to the surface vorticity of the eddy (Eden and Dietze 2009; Seo et al. 2016), while differences between the surface wind and ocean velocities can result in Ekman upwelling and downwelling in the cores of anticyclones and cyclones, respectively. Renault et al. (2016) summarized previous works on the current feedback mechanisms. On one hand, eddy-induced wind stress anomalies produce a stress curl that is opposite to the eddy vorticity, damping the kinetic energy of eddy directly. On the other hand, eddy currents will induce the adjustment in the atmospheric boundary layer and produce wind anomalies that oppose the anomalous wind stress curl, acting to reduce its damping effect on eddies. To date, this eddy–current feedback theory has been supported by recent wind power analyses in the KE region (Xu et al. 2016; Yang and Liang 2018; Yang et al. 2019). In addition to EKE, recent high-resolution satellite observations and coupled atmosphere–ocean model simulations indicate a large potential energy release from mesoscale ocean fronts and eddies to the overlying atmosphere in the North Pacific Ocean (Bishop et al. 2015; Ma et al. 2016; Bishop et al. 2017; Liu et al. 2018; Yang et al. 2019; Shan et al. 2020; Jing et al. 2020). On one hand, strong mesoscale air–sea heat exchange acts as an eddy killer by dissipating eddy potential energy (EPE; Ma et al. 2016; Bishop et al. 2017; Shan et al. 2020). On the other hand, it promotes strong turbulent mixing within the mixing layer and generates vertical

heat transport (Jing et al. 2020). Moreover, Bishop et al. (2017) explored the temporal and spatial dependence of mesoscale air–sea interaction and indicated different dynamics at different time scales: SST variability within synoptic time scales is driven by surface heat flux (SHF) associated with weather variability, whereas at monthly and longer time scales both SST and SHF are driven by internal ocean processes. Yang et al. (2019) further supported this finding using an eddy energetic analysis.

While these previous studies have significantly improved our understanding of ocean mesoscale variability in the KE region and highlighted the role of mesoscale air–sea interactions in mesoscale energy cycle, some important issues remain unsolved. First and most importantly, a detailed picture of the energy budget of mesoscale variability at different time scales remains fragmentary. Second, the role of air–sea interaction in mesoscale energy balance at different time scales has yet to be quantified. These issues pose hindrances to our understanding of the basic mesoscale dynamics in the KE region. In this paper, the abovementioned issues are examined through analyzing an eddy-resolving coupled climate model simulation.

The rest of this paper is organized as follows: section 2 gives a brief description of the datasets and method used in this study. In section 3, a detailed study of air–sea interaction and its role in mesoscale energy balance is presented. The paper ends with a summary and further discussion in section 4.

2. Data and method

a. Data

1) CESM MODEL

In this study, the eddy-resolving model product based on a version of the Community Earth System Model (CESM) is used. This simulation is developed as a part of the Accelerated Scientific Discovery (ASD) initiative conducted by the National Center for Atmospheric Research (NCAR). The global fully coupled model includes the Community Atmosphere Model version 5 (CAM5) with a spectral element dynamical core as the atmospheric component and the Parallel Ocean Program version 2 (POP2) as the oceanic component. A detailed model description is given by Small et al. (2014). As the latest version of the atmosphere model series, the CAM5 is based on a global cubed-sphere grid at horizontal resolution of about 0.25° with 30 pressure levels in the vertical direction. POP2 is a finite-difference code on an Arakawa B grid (velocities are specified at tracer cell corners) with horizontal resolution of 0.1° and 62 z levels in the vertical with increasing grid space from 5 m near the sea surface to 250 m near the bottom. The K-profile parameterization (KPP) vertical mixing scheme (Large et al. 1994) is employed to parameterize the subgrid-scale vertical mixing processes and both biharmonic friction and Laplacian friction are applied in horizontal direction. The ocean and atmosphere components of CESM are connected by a coupling software framework which allows frequent mass, momentum and energy exchanges at the interface. For every 6 h, POP2 offers SST and surface velocity to CAM5 and obtains momentum flux, heat flux and equivalent "salt flux" (calculated based on freshwater flux) from CAM5 on the basis of surface flux scheme developed

by Large and Yeager (2009). The model is integrated for 100 years with 14 years of spinup. In this study, we extended this simulation for 4 more years and saved all the daily mean terms in the momentum and temperature equations (appendix A) to facilitate a detailed energetics analysis. The same CESM dataset has been used by Yang et al. (2019) to diagnose energetics within a time window of 15–270 days in the KE region. In this study, we extend this analysis by dividing eddy energetics and air–sea interaction into two time windows with a cutoff period of about 3 weeks and compare the energy balance and underlying processes between these two time windows. The results presented below is based on the analysis performed in the KE region (140°–170°E, 25°–45°N).

2) OBSERVATIONS

Two observational datasets are used in this study to validate the CESM model output in the region of our interest. For the SST field, we utilize the optimum interpolation sea surface temperature (OISST, https://www.ncdc.noaa.gov/oisst) product maintained operationally at 1-day delay by the National Oceanic and Atmospheric Administration's (NOAA) National Climate Data Center (NCDC). With the application of bias adjustment methodology, it blends the Advanced Very High-Resolution Radiometer (AVHRR) infrared satellite SST data, the Advanced Microwave Scanning Radiometer (AMSR) satellite SST data, and in situ temperature data from ships and buoy measurements (Reynolds et al. 2007). The dataset has a spatial grid resolution of 0.25° and a temporal resolution of 1 day. Here, an 8-yr-long SST product covering the period from December 2003 to November 2011 within the KE region (140°–170°E, 25°–45°N) is used.

To validate the EKE field from the CESM model output, the merged sea surface height (SSH) product derived from measurements of several satellites (e.g., *Jason-1* and *Jason-2*, *Envisat*, *ERS-1* and *ERS-2*) is used in this study. This dataset is provided by Copernicus Marine Environment Monitoring Service (CMEMS, http://marine.copernicus.eu/). The horizontal resolution of the SSH dataset is 0.25° at daily intervals. In our analysis, the SSH fields during 2001–16 within the region (140°E–180°, 25°–45°N) are used.

b. Method

In this study, mesoscale air–sea interaction and energetics in the KE region are analyzed using multiscale energy and vorticity analysis method (MS-EVA; Liang and Robinson 2005; Liang 2016). Based on wavelet analyses (Meyer wavelet is used in this study), MS-EVA decomposes time series into several time-scale windows orthogonally without changing the total energy. Here, we decompose the variables into two windows:

$$A = A^{\sim 0} + A^{\sim 1}, \tag{1}$$

where ~ 0, ~ 1 represent low-frequency and high-frequency processes, respectively. This two-window decomposition method has been employed in previous studies to examine ocean mesoscale energetics (e.g., Yang et al. 2017). Here, the high-frequency processes include the direct oceanic response to synoptic-scale atmospheric processes (e.g., Ekman drift) and mesoscale filaments. The processes, such as mesoscale eddies and jet meanders characterized by longer period, belong to the low-frequency window. The cutoff period is set to be 23 days, which is long enough to cover the synoptic-scale processes (Nakamura et al. 2004; Gan and Wu 2015; McWilliams 2016). Moreover, changing the cutoff period from 17 to 34 days generates no significant differences in relative magnitudes of the energy terms. Therefore, 23 days is chosen as the cutoff period in this study.

The energy equations within the low-frequency window are (Fig. 2a):

$$\rho_0 \frac{\partial}{\partial t} \text{EKE}_0 = \frac{\partial}{\partial t} \rho_0 \frac{(u'^{\sim 0})^2 + (v'^{\sim 0})^2}{2} = \underbrace{-\rho'^{\sim 0} w'^{\sim 0} g}_{\text{BF}^{\sim 0}} \underbrace{- \rho_0 \left[(\mathbf{v} \cdot \nabla u' + v' \cdot \nabla \overline{u})^{\sim 0} u'^{\sim 0} + (\mathbf{v} \cdot \nabla v' + v' \cdot \nabla \overline{v})^{\sim 0} v'^{\sim 0} \right]}_{\text{BT}^{\sim 0}}$$

$$\underbrace{-\nabla \cdot p'^{\sim 0} \mathbf{v}'^{\sim 0}}_{\text{Pres}^{\sim 0}} \underbrace{+ \rho_0 \mathbf{v}_H'^{\sim 0} \cdot (A_{M4} \nabla^4 \mathbf{v}_H' + A_{M2} \nabla^2 \mathbf{v}_H')^{\sim 0}}_{D_{KH}^{\sim 0}} \underbrace{+ \rho_0 \mathbf{v}_H'^{\sim 0} \cdot \left[\frac{\partial}{\partial z} \left(\mu \frac{\partial \mathbf{v}_H}{\partial z} \right) \right]'^{\sim 0}}_{D_{KV}^{\sim 0}}, \underbrace{}_{D_K^{\sim 0}} \tag{2a}$$

$$\frac{\partial}{\partial t} \frac{(T'^{\sim 0})^2}{2} = \underbrace{-(\mathbf{v} \cdot \nabla T' + v' \cdot \nabla \overline{T})^{\sim 0} T'^{\sim 0}}_{\text{BC}_{\text{temp}}^{\sim 0}} \underbrace{- T'^{\sim 0} w'^{\sim 0} \frac{\partial T_0(z)}{\partial z}}_{\text{BF}_{\text{temp}}^{\sim 0}}$$

$$\underbrace{+ T'^{\sim 0} (A_{H4} \nabla^4 T' + A_{H2} \nabla^2 T')^{\sim 0}}_{D_{\text{temp}H}^{\sim 0}} \underbrace{+ T'^{\sim 0} \left(\frac{\partial}{\partial z} \left\{ \kappa \frac{\partial [T + T_0(z)]}{\partial z} \right\}' + F_T' \right)^{\sim 0}}_{D_{\text{temp}V}^{\sim 0}}. \underbrace{}_{D_{\text{temp}}^{\sim 0}} \tag{2b}$$
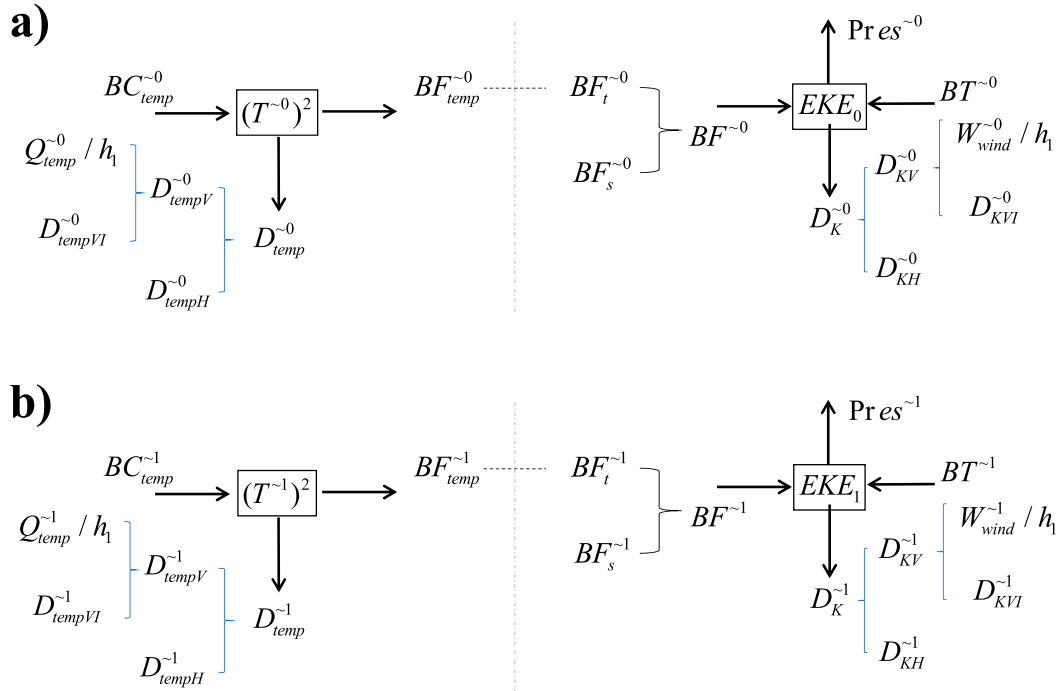
FIG. 2. Schematic of the eddy energy budget.

In Eq. (2), overbar and prime denote mean flow and mesoscale variability, respectively. The terms $\mathbf{v} = (u, v, w)$ and $\mathbf{v}_H = (u, v)$ represent the full and horizontal velocity vectors, respectively. The term T is the potential temperature perturbation from the background profile $T_0(z)$, and F_T represents the nonlocal T transport due to the entrainment process parameterized using the KPP mixing scheme (Large et al. 1994). Parameter ρ is the density with reference value ρ_0 (1025 kg m^{-3}), and p indicates pressure. The Laplacian viscosity (diffusion) coefficient A_{M2} (A_{H2}) is set as 10^4 m^2 s^{-1} (10^4 m^2 s^{-1}), and the biharmonic viscosity (diffusion) coefficient A_{M4} (A_{H4}) is set as 27×10^9 m^4 s^{-1} (3×10^9 m^4 s^{-1}). Parameters κ and μ are the corresponding vertical mixing coefficients, which depend on the local state and mixing parameterization. The operator ∇

represents the three-dimensional gradient operator. Detailed derivations of Eq. (2) are given in appendix A. In Eq. (2a), $-\rho'^{\sim 0} w'^{\sim 0} g$, the first term on the right-hand side, describes conversion of EPE to EKE through vertical buoyancy forcing (BF$^{\sim 0}$). The second term $-\rho_0[(\mathbf{v} \cdot \nabla u' + v' \cdot \nabla \overline{u})^{\sim 0} u'^{\sim 0} + (\mathbf{v} \cdot \nabla v' + v' \cdot \nabla \overline{v})^{\sim 0} v'^{\sim 0}]$ denotes the mesoscale energy fed into the domain through advection and interaction between barotropic mean flow and variability (BT$^{\sim 0}$). Once generated, EKE is transported out of the domain by pressure work (Pres$^{\sim 0}$), or balanced by energy dissipation $D_K^{\sim 0}$ through friction, wind stress, and bottom drag. Here, $D_K^{\sim 0}$ can be divided into horizontal friction ($D_{KH}^{\sim 0}$) and vertical mixing ($D_{KV}^{\sim 0}$) components, while $D_{KV}^{\sim 0}$ can be further divided into surface forcing ($W_{\text{wind}}^{\sim 0}$) and oceanic mixing components:

$$
\begin{aligned}
D_{KV}^{\sim 0} &= \rho_0 \mathbf{v}_H'^{\sim 0} \cdot \left[\frac{\partial}{\partial z} \left(\mu \frac{\partial \mathbf{v}_H}{\partial z} \right)' \bigg|_{\text{ocean}} \right]^{\sim 0} + \rho_0 \mathbf{v}_H'^{\sim 0} \cdot \left[\frac{\partial}{\partial z} \left(\mu \frac{\partial \mathbf{v}_H}{\partial z} \right)' \bigg|_{\text{surface}} \right]^{\sim 0} \\
&= \rho_0 \mathbf{v}_H'^{\sim 0} \cdot \left[\frac{\partial}{\partial z} \left(\mu \frac{\partial \mathbf{v}_H}{\partial z} \right)' \bigg|_{\text{ocean}} \right]^{\sim 0} + \rho_0 \mathbf{v}_H'^{\sim 0} |_{\text{surface}} \cdot \frac{\tau'^{\sim 0}}{\rho_0 h_1} \\
&= D_{KVI}^{\sim 0} + \frac{W_{\text{wind}}^{\sim 0}}{h_1},
\end{aligned}
\tag{3}
$$

where h_1 represents the depth of the first level (10 m in CESM), $\mathbf{v}_{H\text{surface}}$ is the surface horizontal velocity and τ represents the surface wind stress. Physically, $W_{\text{wind}}^{\sim 0}$ denotes wind power input whereas $D_{KVI}^{\sim 0}$ involves the oceanic friction and bottom drag processes.

Equation (2b) describes the sources and sinks for temperature (T variance) and is closely related to EPE. Following Yang

et al. (2019), the classic EPE equation based on density field (Lornez 1955) is not used here. This is because in the classic definition, terms in the EPE equation are divided by buoyancy frequency (N^2) that is close to zero near the sea surface. Therefore, large uncertainties will be introduced in the estimation of air–sea interaction. Furthermore, temperature equation is

prognostically determined by CESM and saved as model output, especially for the vertical dissipation term. As such, energetics analysis can be carried out more accurately by directly using the T-variance equation rather than the density-based EPE equation. Besides the evolution of temperature, variability of salinity may also affect the mesoscale processes in the North Pacific (Jing et al. 2019). Based on the approximate equation of state in the ocean for CESM model (Smith et al. 2010), it is found that the role of salinity variation in regulating

the mesoscale energy balance is secondary in the KE region (appendix B). Therefore, we will focus on T variance in the following. According to Eq. (2b), the low-frequency change of T variance is regulated by baroclinic conversion and advection ($BC_{temp}^{\sim 0}$), mesoscale temperature induced EPE-to-EKE conversion ($BC_{temp}^{\sim 0}$) and dissipation ($D_{temp}^{\sim 0}$). The $D_{temp}^{\sim 0}$ term includes energy dissipation within the ocean interior due to mixing and diffusion processes and at the air–sea interface due to heat exchange with the atmosphere:

$$
\begin{aligned}
D_{temp}^{\sim 0} &= T'^{\sim 0}\left(A_H \nabla^4 T' + A_{H2}\nabla^2 T' + \frac{\partial}{\partial z}\left\{\kappa \frac{\partial[T+T_0(z)]}{\partial z}\right\}'\bigg|_{ocean} + F_T'\right)^{\sim 0} + T'^{\sim 0}\left(\frac{\partial}{\partial z}\left\{\kappa \frac{\partial[T+T_0(z)]}{\partial z}\right\}'\bigg|_{surface}\right)^{\sim 0} \\
&= T'^{\sim 0}(A_{H4}\nabla^4 T' + A_{H2}\nabla^2 T')^{\sim 0} + T'^{\sim 0}\left(\frac{\partial}{\partial z}\left\{\kappa \frac{\partial[T+T_0(z)]}{\partial z}\right\}'\bigg|_{ocean} + F_T'\right)^{\sim 0} + SST'^{\sim 0}\times \frac{Q_{net}'^{\sim 0}}{C_p \rho_0 h_1} \\
&= D_{tempH}^{\sim 0} + D_{tempVI}^{\sim 0} + \frac{\Theta_{temp}^{\sim 0}}{h_1}.
\end{aligned}
\tag{4}
$$

Here Q_{net} is the net surface heat flux, C_p denotes the specific heat of seawater, h_1 represents the depth of the first level. In the above equation, $\Theta_{temp}^{\sim 0}$ represents dissipation at the air–sea interface due to heat exchange with the atmosphere, while

$D_{tempH}^{\sim 0}$ ($D_{tempVI}^{\sim 0}$) is horizontal (vertical) mixing and diffusion processes within the ocean interior.

By replacing ~ 0 with ~ 1, we obtain the energy equations within the high-frequency window (Fig. 2b):

$$
\rho_0 \frac{\partial}{\partial t}EKE_1 = \frac{\partial}{\partial t}\rho_0 \frac{(u'^{\sim 1})^2 + (v'^{\sim 1})^2}{2} = \underbrace{-\rho'^{\sim 1}w'^{\sim 1}g}_{BF^{\sim 1}} \underbrace{-\rho_0\left[(\mathbf{v}\cdot\nabla u' + v'\cdot\nabla\overline{u})^{\sim 1}u'^{\sim 1} + (\mathbf{v}\cdot\nabla v' + v'\cdot\nabla\overline{v})^{\sim 1}v'^{\sim 1}\right]}_{BT^{\sim 1}}
$$

$$
\underbrace{-\nabla\cdot\rho'^{\sim 1}\mathbf{v}'^{\sim 1}}_{Pres^{\sim 1}} \underbrace{\underbrace{+\rho_0\mathbf{v}_H'^{\sim 1}\cdot(A_{M4}\nabla^4\mathbf{v}_H' + A_{M2}\nabla^2\mathbf{v}_H')^{\sim 1}}_{D_{KH}^{\sim 1}} + \underbrace{\rho_0\mathbf{v}_H'^{\sim 1}\cdot\left[\frac{\partial}{\partial z}\left(\mu\frac{\partial\mathbf{v}_H}{\partial z}\right)\right]^{\sim 1}}_{D_{KV}^{\sim 1}}}_{D_K^{\sim 1}},
\tag{5a}
$$

$$
\frac{\partial}{\partial t}\frac{(T'^{\sim 1})^2}{2} = \underbrace{-(\mathbf{v}\cdot\nabla T' + v'\cdot\nabla\overline{T})^{\sim 1}T'^{\sim 1}}_{BC_{temp}^{\sim 1}} \underbrace{-T'^{\sim 1}w'^{\sim 1}\frac{\partial T_0(z)}{\partial z}}_{BF_{temp}^{\sim 1}}
$$

$$
\underbrace{\underbrace{+T'^{\sim 1}(A_{H4}\nabla^4 T' + A_{H2}\nabla^2 T')^{\sim 1}}_{D_{tempH}^{\sim 1}} + \underbrace{T'^{\sim 1}\left(\frac{\partial}{\partial z}\left\{\kappa\frac{\partial[T+T_0(z)]}{\partial z}\right\}' + F_T'\right)^{\sim 1}}_{D_{tempV}^{\sim 1}}}_{D_{temp}^{\sim 1}}.
\tag{5b}
$$

Similarly, we also have the air–sea interaction terms associated with wind power input

$$
W_{wind}^{\sim 1} = \mathbf{v}_H'^{\sim 1}\big|_{surface}\cdot\tau^{\sim 1},
\tag{6}
$$

and air–sea heat exchange

$$
\Theta_{temp}^{\sim 1} = SST'^{\sim 0}\times\frac{Q_{net}'^{\sim 0}}{C_p\rho_0}.
\tag{7}
$$

3. Energetics analysis

a. Model validation

Before exploring the dynamics, it is necessary to quantify whether CESM can accurately capture the mesoscale activity in the KE region. Figure 3 compares the time-mean surface EKE and T-variance fields derived from CESM and observation. The EKE patterns within the two windows derived from CESM
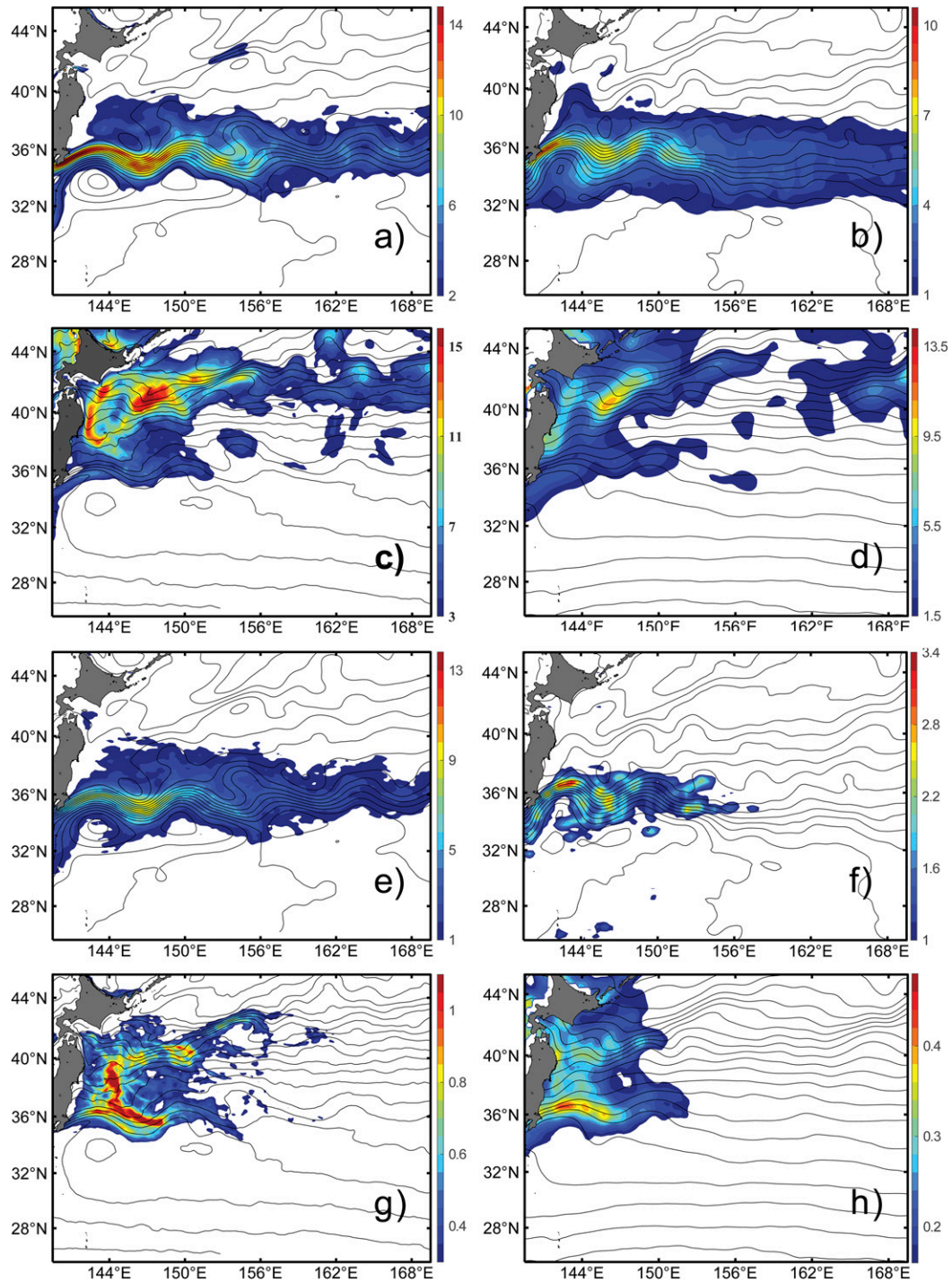
FIG. 3. Time-mean surface EKE_0 field based on (a) CESM and (b) CMEMS (colored shading; $0.1\,\mathrm{m^2\,s^{-2}}$). Contours denote the mean SSH field. Time-mean surface $(T'^{\sim 0})^2$ field based on (c) CESM and (d) OISST (colored shading; degrees squared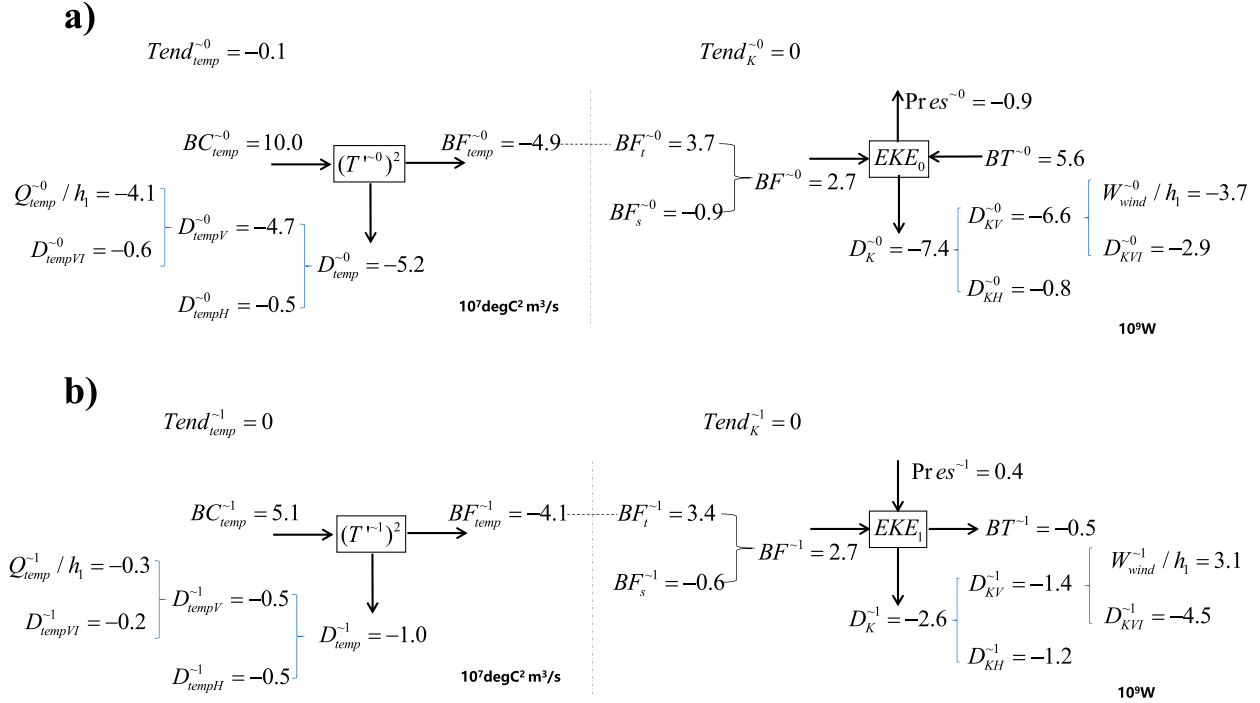). Contours denote the mean SST field. Time-mean surface EKE_1 field based on (e) CESM and (f) CMEMS (colored shading; $0.01\,\mathrm{m^2\,s^{-2}}$). Contours denote the mean SSH field. Time-mean surface $(T'^{\sim 1})^2$ field based on (g) CESM and (h) OISST (colored shading; degrees squared). Contours denote mean SST field.

a)

b)

FIG. 4. Eddy energy budget for (a) $(T'^{\sim 0})^2$ and EKE_0, and (b) $(T'^{\sim 1})^2$ and EKE_1 in the upper 200-m KE region (150°–170°E, 32°–42°N) derived from CESM.

resemble those from satellite observations. In the upstream, the mean path of the KE is characterized by the presence of two quasi-stationary meanders with their ridges located at around 144° and 150°E, respectively. Along with the meanders, the upstream KE is found to be rich in mesoscale variability (Figs. 3a,e). Compared to the upstream KE west of 150°E, the downstream KE exhibits a relative straight path and weaker mesoscale variability (Figs. 3b,f).

Besides the circulation change, the KE region is also abundant with temperature variability. Different from the EKE field, the T variance is characterized with large values along the Oyashio Extension (~40°N) and Japan coast between 38° and 42°N, as well as along the KE jet, especially within the low-frequency window (Figs. 3c,d). The large T variance along the Japan coast is associated with the southward intrusion of the Oyashio Current (Qiu 2001; Yasuda 2003). The magnitudes of T variance and EKE derived from CESM are larger than those from observations, which may be caused by the higher resolution of CESM. To demonstrate this, a 0.3° × 0.3° (9 points) and 3-day average are applied to the CESM velocity/temperature field. The resultant magnitudes of both EKE and T variance are found to be more comparable to each other between CESM and observations (not shown). Overall, this suggests that CESM can realistically simulate the current and temperature structures of the mesoscale variability in the KE region. In the following discussion, we will examine its mesoscale energy balance through budget analysis.

b. Mesoscale energy budget

Figure 4 summarizes the budget for EKE and T variance within two windows in the upper 200 m layer in the region of (150°–170°E, 32°–42°N) derived from CESM. Changing the integration depth from 150 to 250 m induces no significant difference in the results because all the terms are relatively small beneath 150 m. To get a better understanding of the dynamics, the horizontal distributions (Figs. 5 and 6) of the energy terms are also provided. Figure 5a shows a significant baroclinic energy conversion to $(T'^{\sim 0})^2$ to the northern side of KE, especially near the meander around 156°E. The generated energy is either fed into EKE_0 through vertical flux ($BF_{temp}^{\sim 0}$) or dissipated through dissipation processes ($D_{temp}^{\sim 0}$). Same as $BC_{temp}^{\sim 0}$, both of them depict meridional variation with maximum occupying the area north of the KE jet (Figs.5b,c). A positive spot is seen at (152°E, 35°N) in Fig. 5b, which may be caused by the vertical velocity anomaly related to the recurring passages of the quasi-steady meander (Bishop 2013). Besides along the KE jet, significant $D_{temp}^{\sim 0}$ can also be found around the Oyashio Extension. Quantitatively, $BF_{temp}^{\sim 0}$ and $D_{temp}^{\sim 0}$ contribute equally to the total T-variance sink. Air–sea heat exchange plays an important role in the budget and contributes to ~80% of $D_{temp}^{\sim 0}$ and ~40% of the total energy production (Fig. 4a), in accordance with previous studies (Ma et al. 2016). It is noted that the damping role of $\Theta_{temp}^{\sim 0}$ is much larger here than that from Yang et al. (2019). This is because the domain we conduct budget analysis in this study mainly locates on the northern side of the KE jet where air–sea heat exchange is more active. Moreover, Yang et al. (2019) focuses on the upstream KE close to Japan coast. In that region, both baroclinic energy generation and horizontal diffusion is larger than the downstream area used here, which will reduce the contribution of air–sea interaction in energy balance as well. Different from $(T'^{\sim 0})^2$, the budget of high-frequency T variance is characterized by the
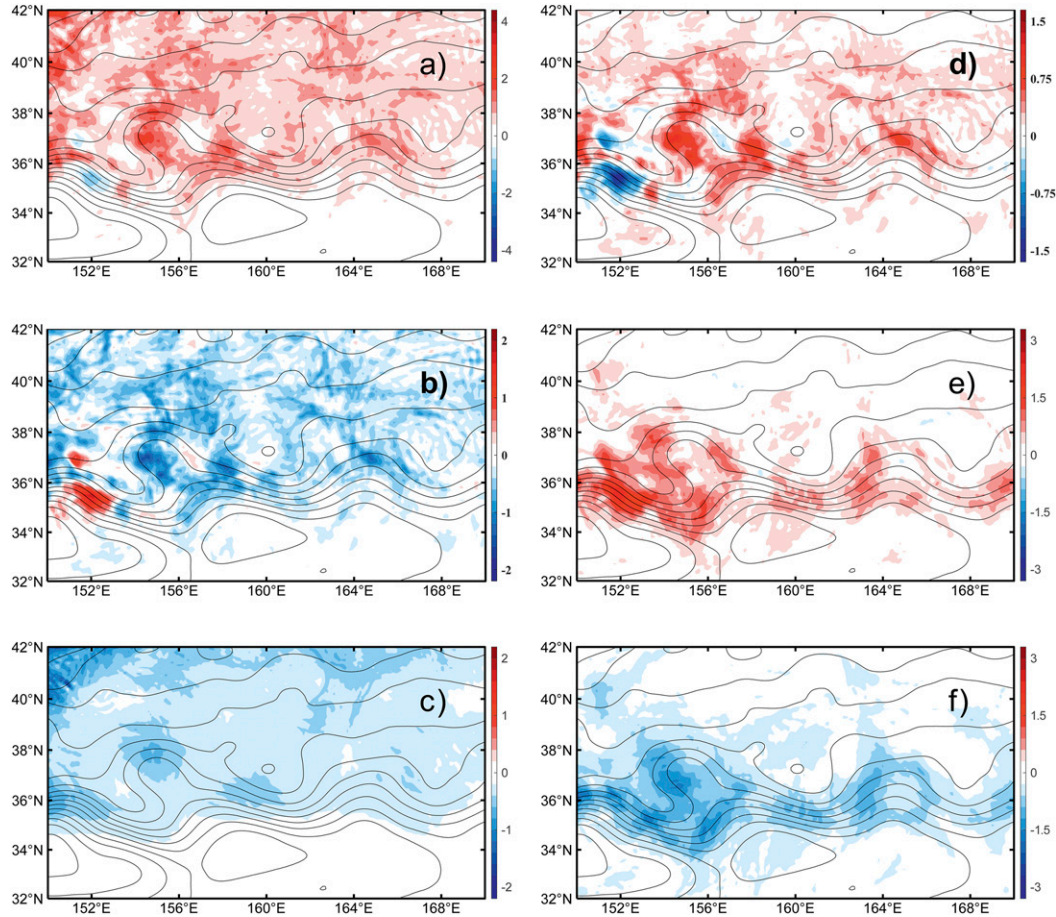
FIG. 5. Horizontal distribution of (a) $BC_{temp}^{\sim 0}$ (colored shading; $10^{-4}\,°C^2\,m\,s^{-1}$), (b) $BF_{temp}^{\sim 0}$ (colored shading; $10^{-4}\,°C^2\,m\,s^{-1}$), (c) $D_{temp}^{\sim 0}$ (colored shading; $10^{-4}\,°C^2\,m\,s^{-1}$), (d) $BF^{\sim 0}$ (colored shading; $0.01\,W\,m^{-2}$), (e) $BT^{\sim 0}$ + $Pres^{\sim 0}$ (colored shading; $0.01\,W\,m^{-2}$) and (f) $D_K^{\sim 0}$ (colored shading; $0.01\,W\,m^{-2}$) integrated over the upper 200 m derived from CESM. Contours are mean SSH isolines.

quasi-balance between $BC_{temp}^{\sim 1}$ and $BF_{temp}^{\sim 1}$ (Fig. 4b), which can also be revealed by their consistent patterns and magnitudes in Figs. 6a and 6b. In addition to the energy balance, a comparison between $BF_{temp}^{\sim 0}$ and $BF_{temp}^{\sim 1}$ further indicates that the low-frequency and high-frequency vertical buoyancy fluxes are equally important in regulating the EKE. The contribution of $\Theta_{temp}^{\sim 1}$ is negligible, which suggests that the balance of $(T'^{\sim 1})^2$ cannot be directly regulated by high-frequency air–sea heat flux forcing.

In addition to the EPE_0-to-EKE_0 conversion, mesoscale eddies also draw their kinetic energy from the mean flow through $BT^{\sim 0}$ (Fig. 5e), especially near the meanders of the KE jet (35°N, 152°E). This phenomenon is associated with the along-jet variation of meridional relative PV gradient (Waterman and Jayne 2011). Integrating over the KE (Fig. 4a), $BF^{\sim 0}$ and $BT^{\sim 0}$ contribute about 1/3 and 2/3 to the total EKE_0 source, respectively. The generated EKE is either transported out of the domain by the pressure work $Pres^{\sim 0}$ (11%) or dissipated through dissipation processes $D_K^{\sim 0}$ (89%). Wind work acts as an energy sink on the eddies and accounts for ~50% of EKE dissipation and ~45% of the total EKE generation, consistent with previous

estimations (Gaube et al. 2015; Renault et al. 2016, 2017; Xu et al. 2016; Yang and Liang 2018). Compared to its low-frequency counterpart, the balance of EKE_1 is dominated by $BF^{\sim 1}$ and $D_K^{\sim 1}$, with the role of $BT^{\sim 1}$ and $Pres^{\sim 1}$ secondary (Fig. 4b, Figs. 6d–f). Different from its counterpart in low-frequency window, the role of $D_{KH}^{\sim 1}$ cannot be directly neglected. Moreover, it is found that the wind work for periods shorter than ~3 weeks is positive rather than negative, suggesting that the high-frequency wind work is forcing rather than damping EKE.

The mesoscale energy balance is further explored by analyzing the time evolution. It is revealed from Fig. 7 that all the energy sources and sinks are characterized with obvious seasonal cycle with maximum occurring in winter. In $(T'^{\sim 0})^2$ balance (Fig. 7a), the generated energy through $BC_{temp}^{\sim 0}$ is mainly balanced by $BF_{temp}^{\sim 0}$ and $D_{temp}^{\sim 0}$ in winter, and it is reflected as the tendency of T variance in summer. In addition, $BF_{temp}^{\sim 0}$ is found to change in pace with $D_{temp}^{\sim 0}$. Their correlation approaches 0.9 and is significant at the 99% confidence level (the degrees of freedom for the low-passed time series are evaluated based on the Monte Carlo test; hereinafter, all correlations are found to be significant at the 99% confidence level), indicating the dynamical link between
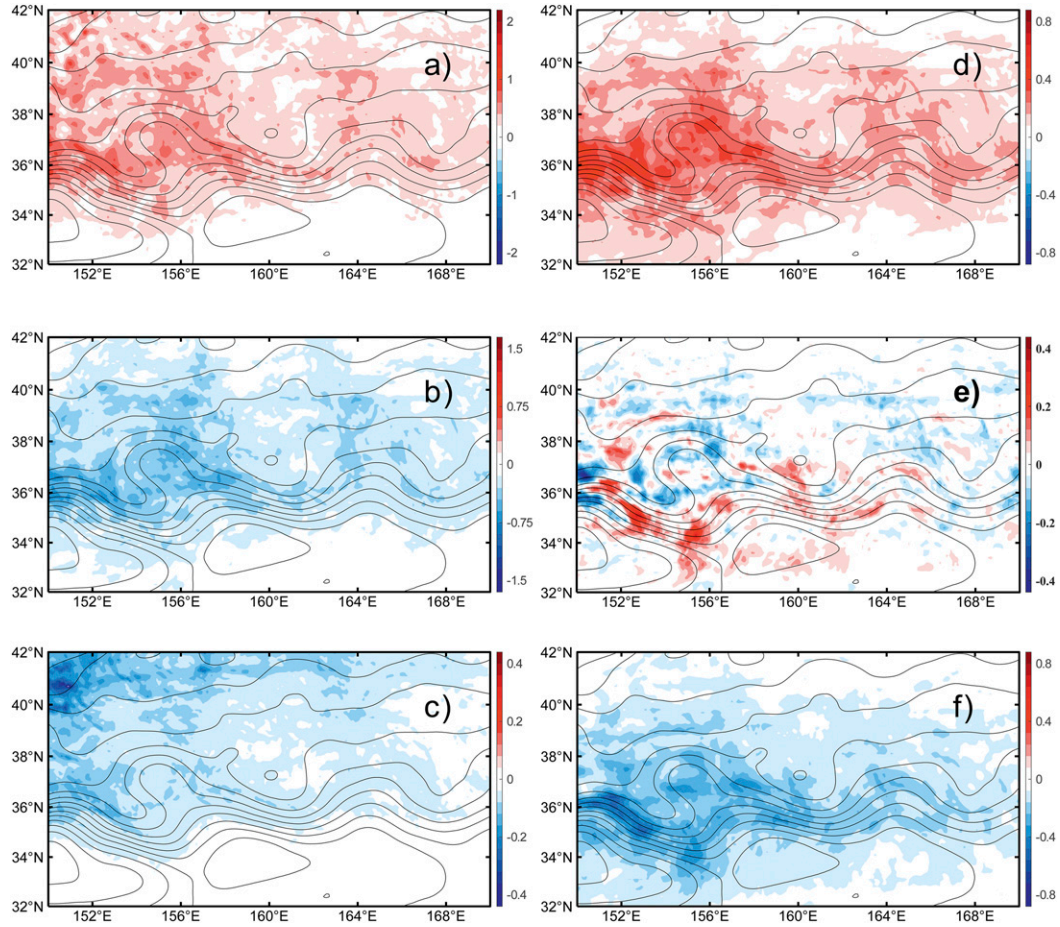
FIG. 6. As in Fig. 5, but within the high-frequency window.

vertical mixing and heat transport. Compared to $(T'^{~0})^2$ tendency, the tendency of EKE_0 is always smaller compared to other terms (Fig. 7b). Both $BF^{~0}$ and $BT^{~0}$ show significant correlations with $D_K^{~0}$ with the linear correlation coefficient exceeding 0.75.

Within the high-frequency window (Figs. 7c,d), the time evolution of the budget is more intuitive, especially in winter.

Combined with the analysis in Figs. 4a and 4b mesoscale energy pathway consisting of $BC_{temp}^{~1} \rightarrow BF_{temp}^{~1}$ ($BF^{~1}$) $\rightarrow D_K^{~1}$ is detected. This suggests that the high-frequency baroclinic energy is mainly released to kinetic energy and finally balanced by mixing process. To better understand the EKE_1 budget, we apply below the turbulent thermal wind (TTW) theory that
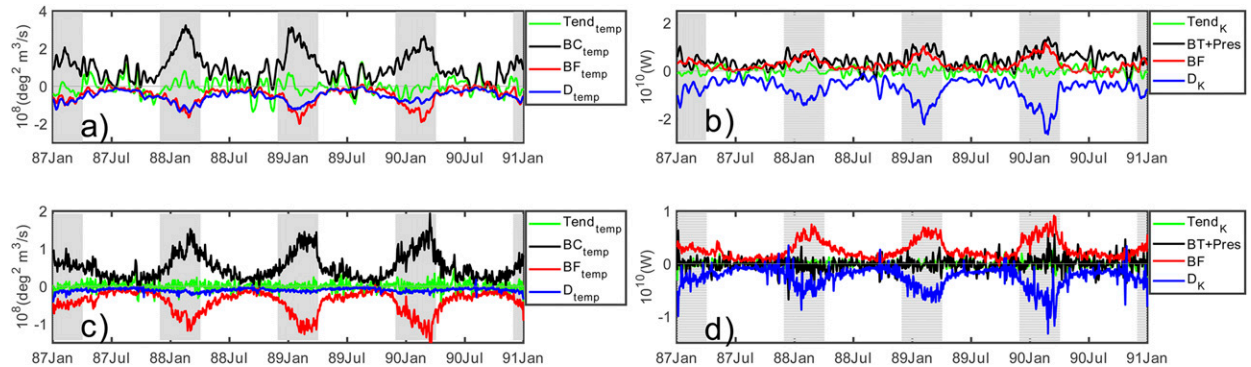
FIG. 7. Time evolution of energy budget in the upper 200-m KE region (150°–170°E, 32°–42°N) for (a) $(T'^{~0})^2$, (b) EKE_0, (c) $(T'^{~1})^2$, and (d) EKE_1. Shading indicates boreal winter (December–March).
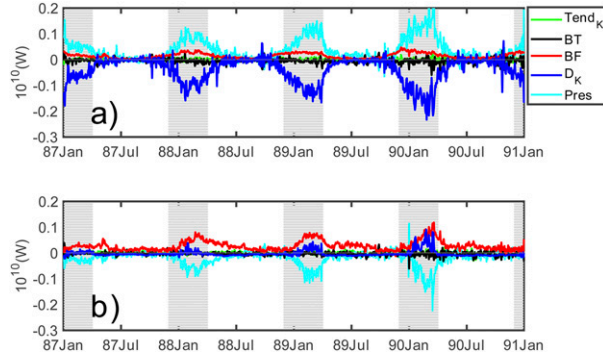
FIG. 8. Time evolution of energy budget for EKE_1 in the KE region (150°–170°E, 32°–42°N) at (a) 25 and (b) 135 m. Shading indicates boreal winter.

involves both vertical mixing and thermal wind balance (Gula et al. 2014; McWilliams 2016):

$$-fv = -\frac{1}{\rho_0}\frac{\partial p}{\partial x} + \left(A_{M4}\nabla^4 u + A_{M2}\nabla^2 u + \frac{\partial}{\partial z}\mu\frac{\partial u}{\partial z} \right), \quad (8a)$$

$$fu = -\frac{1}{\rho_0}\frac{\partial p}{\partial y} + \left(A_{M4}\nabla^4 v + A_{M2}\nabla^2 v + \frac{\partial}{\partial z}\mu\frac{\partial v}{\partial z} \right). \quad (8b)$$

Based on these equations and momentum analysis, Gula et al. (2014) reported that the baroclinic energy stored in the horizontal buoyancy gradient can be released by vertical mixing. Here, we modify the equation by considering both the horizontal viscosity and vertical viscosity as the contribution of horizontal viscosity to energy balance cannot be neglected (Fig. 4). Using the same derivation process for Eq. (5a), we obtain the energy budget associated with the TTW balance:

$$-\rho'^{\sim 1} w'^{\sim 1} g - \nabla \cdot \rho'^{\sim 1} \mathbf{v}'^{\sim 1}$$
$$+ \rho_0 \mathbf{v}_H'^{\sim 1} \cdot \left[A_{M4}\nabla^4 \mathbf{v}_H' + A_{M2}\nabla^2 \mathbf{v}_H' + \frac{\partial}{\partial z}\left(\mu\frac{\partial \mathbf{v}_H}{\partial z} \right)' \right]^{\sim 1} = 0. \quad (9)$$

Equation (9) predicts the energy balance between $Pres^{\sim 1}$, $BF^{\sim 1}$, and $D_K^{\sim 1}$, resembling the results in Figs. 4 and 7. To support the applicability of TTW in this problem, the time evolution of the area-mean budget of EKE_1 within the domain (150°–170°E, 32°–42°N) at 25 and 135 m is plotted. Figure 8 reveals that the energy budgets at both depths are characterized by a balance between pressure work, vertical buoyancy forcing and dissipation, while the amplitude of barotropic production and tendency are much smaller. At 25 m, the main energy source is vertical energy flux from surface associated with pressure work, most of which is dissipated directly. In contrast, the buoyancy flux at 135 m is relatively prominent and accounts for the EKE_1 generation. The generated energy is transported away by pressure work. Overall, these evidences indicate that the energy budget of EKE_1 can be attributed to the TTW theory.

According to the above discussion, it is noted that the mesoscale air–sea interaction presents different characteristics and roles in energy balance within the low-frequency
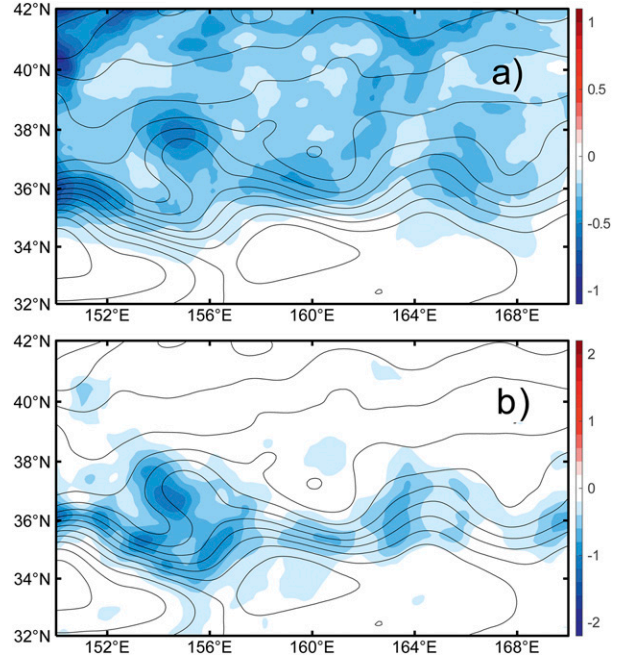

FIG. 9. Horizontal distribution of (a) $\Theta_{temp}^{\sim 0}$ (colored shading; 10^{-4} °C^2 m s^{-1}) and (b) $W_{wind}^{\sim 0}$ (colored shading; 10^{-2} W m^{-2}) derived from CESM. Contours are mean SSH isolines.

and high-frequency bands. To understand the underlying dynamics further, we examine the two frequency bands separately in the following.

c. Air–sea interaction and its potential role

Figure 9a shows the horizontal distribution of $\Theta_{temp}^{\sim 0}$ derived from CESM. Strong mesoscale air–sea interaction is found in the domain, especially on the northern side of KE jet where warm eddies and meanders are generally formed (Sasaki and Minobe 2015). Once generated, these mesoscale processes with higher SST and surface specific humidity are exposed to colder and drier overlying air and can promote latent and sensible heat exchanges (Ma et al. 2016; Large and Yeager 2009). Moreover, the northwesterly wind during winter is stronger on the northern side of the KE jet, which intensifies the meridional difference. In addition to the heat exchange, momentum exchange between atmosphere and oceanic eddies is also prominent. Figure 9b depicts the distribution of wind power input, in which $W_{wind}^{\sim 0}$ exhibits negative values along the KE jet. This indicates that wind forcing acts to spin down the oceanic mesoscale variability, consistent with previous studies (Renault et al. 2016; Xu et al. 2016; Yang and Liang 2018).

The evolution of mesoscale air–sea exchange leaves footprints on energy dissipation. A correlation analysis indicates that there is a significant linear relationship between surface energy flux $\Theta_{temp}^{\sim 0}$ and oceanic energy dissipation $D_{temp}^{\sim 0}$ (correlation coefficient exceeds 0.9). To further explore this relationship, a wavelet coherence analysis is employed. Figure 10a reveals that the coherence always approaches 1 within the low-frequency window, suggesting that the air–sea heat exchange dominates
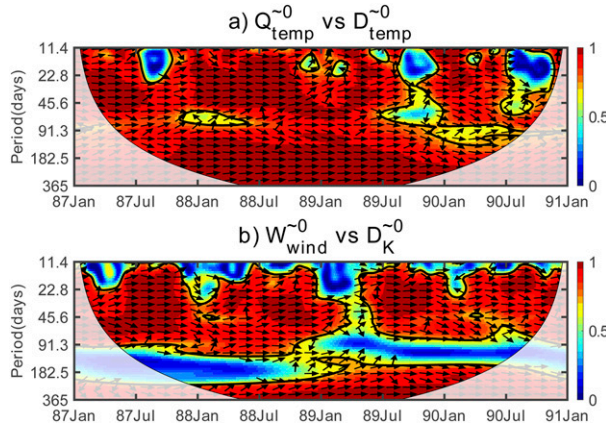
FIG. 10. Wavelet coherence between (a) $\Theta_{\text{temp}}^{\sim 0}$ and upper-200-m integrated $D_{\text{temp}}^{\sim 0}$ and (b) $W_{\text{wind}}^{\sim 0}$ and upper-200-m integrated $D_K^{\sim 0}$. The coherence significant at the 95% significance level is enclosed by the black solid lines. The arrow indicates the phase lag with pointing rightward (leftward) corresponds to the simultaneous positive (negative) correlation.

the *T*-variance dissipation. Similarly, $W_{\text{wind}}^{\sim 0}$ is found to be important in regulating the EKE dissipation as well (Fig. 10b). It is noted that the correlation between $W_{\text{wind}}^{\sim 0}$ and $D_K^{\sim 0}$ is relatively small within the 90–180-day window, implying that ocean interior processes dominate the EKE dissipation in this frequency band. Physically, the energy dissipation is affected by air–sea interaction through two ways. On one hand, wind stress and heat flux can affect the vertical shear of velocity and change temperature field near the sea surface directly. On the other hand, mixing coefficients (μ and κ) can be regulated by the surface air–sea exchange as well. Linear correlation between μ/κ and the surface heat flux/wind stress exceed 0.7. Further analysis based on wavelet coherence reveals that the role of air–sea interaction in influencing μ and κ is more significant during winter when the air–sea temperature difference is large and wind is strong (coherence approaches 1, not shown), consistent with the result from Shan et al. (2020). Moreover, the ratio between the air–sea interaction terms and depth-integrated energy dissipation from sea surface is also calculated. It is found that the contribution of $\Theta_{\text{temp}}^{\sim 0}$ ($W_{\text{wind}}^{\sim 0}$) to depth-integrated $D_{\text{temp}}^{\sim 0}$ ($D_K^{\sim 0}$) decreases steadily as the integration depth increases and reaches to a constant value at 150 m. This value gives an estimated maximal influence depth of $\Theta_{\text{temp}}^{\sim 0}$ ().

Compared to its counterpart in the low-frequency window, air–sea interaction within the high-frequency window depicts different characteristics. Parameter $\Theta_{\text{temp}}^{\sim 1}$ acts as an energy sink in the budget but is characterized by a very small magnitude. Integrating over the domain, it accounts for only 6% of the baroclinic energy generation (Fig. 4), much smaller than that of $\Theta_{\text{temp}}^{\sim 0}$. This phenomenon may be caused by the large thermal inertia of the ocean. Parameter $W_{\text{wind}}^{\sim 1}$ has a positive value in the KE region, which is different from $W_{\text{wind}}^{\sim 0}$. To further explain the underlying dynamics, the mesoscale velocity $\mathbf{v}_H' = (u', v')$ is decomposed into a geostrophic ($\mathbf{v}_{Hg}'$; derived from mesoscale SSH) and an ageostrophic ($\mathbf{v}_{Ha}'$) component. Then $W_{\text{wind}}^{\sim 1}$ is calculated using $\mathbf{v}_{Hg}'$ and $\mathbf{v}_{Ha}'$ separately. It is found that 99% of
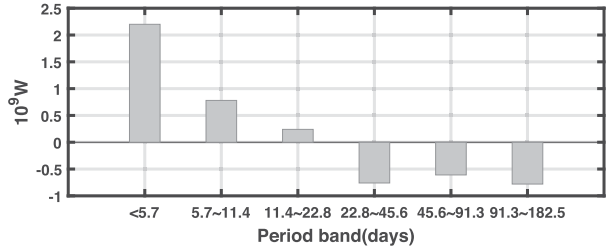

FIG. 11. Change of W_{wind} vs period.

$W_{\text{wind}}^{\sim 1}$ comes from the ageostrophic component, whereas the contribution from geostrophic component is negligible. This indicates that the high-frequency wind power is largely associated with the wind-driven Ekman drift and does not have much direct impact on geographic flow, which is different from the low-frequency window where $W_{\text{wind}}^{\sim 0}$ is dominated by geostrophic component. As such, $W_{\text{wind}}^{\sim 1}$ is not expected to have any major impact on geostrophic mesoscale eddy energetic. However, synoptic wind stresses, rather than dissipating the mesoscale energy directly, may regulate $D_K^{\sim 1}$ through vertical mixing or $\text{Pres}^{\sim 1}$ during the downfront/upfront wind process (Small et al. 2008; Taylor and Ferrari 2010), and further influence the vertical buoyancy flux ($\text{BF}^{\sim 1}$). Nevertheless, linear correlation coefficients between $W_{\text{wind}}^{\sim 1}$ and $D_K^{\sim 1}$, $\text{Pres}^{\sim 1}$, and $\text{BF}^{\sim 1}$ are only -0.2, 0.4, and 0.3, respectively. Combined with the discussion in section 3b, it can be concluded that the role of $W_{\text{wind}}^{\sim 1}$ in regulating the evolution of mesoscale eddy energy balance is secondary, despite its large magnitude.

The above discussion indicates that W_{wind} changes sign within different windows and it is important to know the transition time scale. Figure 11 shows the change of W_{wind} as a function of periods varying from less than 5.7 to 182.5 days. It is found that W_{wind} undergoes a sign change at 22.8 days and implies a different behavior of air–sea interaction dynamics. In the high-frequency band, atmospheric synoptic variability and storms directly influence surface Ekman flow in the ocean, producing positive wind work but little influence on geostrophic mesoscale eddies, whereas within the low-frequency window the wind work draw energy from mesoscale eddies.

4. Summary

Based on the 4-yr daily mean output of high-resolution CESM simulation, mesoscale energetics and air–sea interaction within the two time-scale windows in the Kuroshio Extension region are explored in this study. The major results of this study are summarized as follows:

1) Within the low-frequency window (with period longer than 3 weeks), mesoscale oceanic variability is found to obtain its energy from both the baroclinic and barotropic pathways in the KE region. In comparison, the baroclinic pathway associated with the temperature variability is found to be the main mesoscale energy source in the high-frequency window. All energy sources and sinks show significant seasonal cycles with maximum occurring in winter.
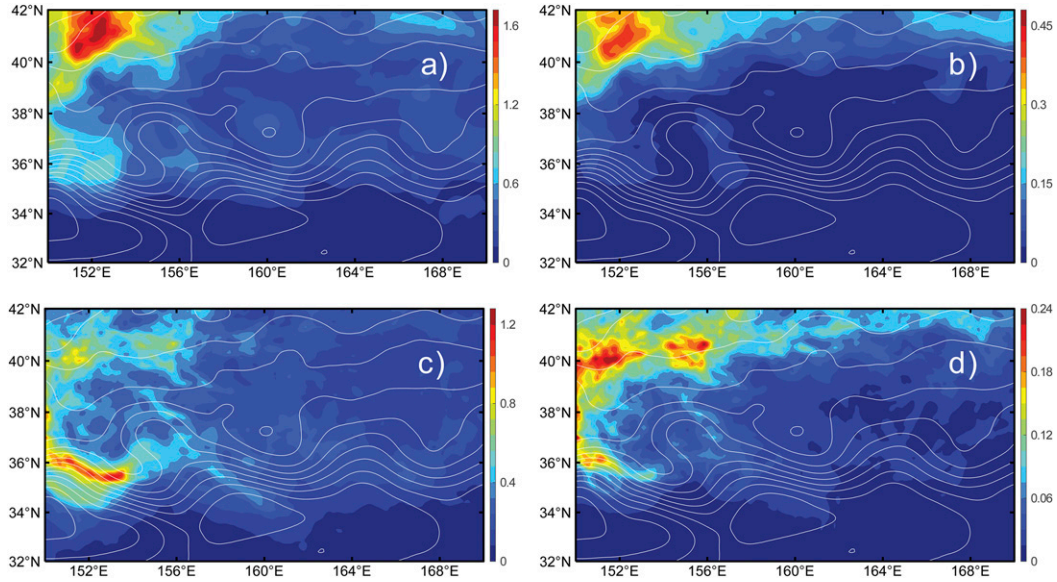
FIG. B1. Horizontal distribution of depth-mean (a) $(\alpha T'^{\sim 0})^2$ [colored shading; $(\text{kg m}^{-3})^2$], (b) $(\beta S'^{\sim 0})^2$ [colored shading; $(\text{kg m}^{-3})^2$], (c) $(\alpha T'^{\sim 1})^2$ [colored shading; 0.1 $(\text{kg m}^{-3})^2$], and (d) $(\beta S'^{\sim 1})^2$ [colored shading; 0.1 $(\text{kg m}^{-3})^2$] in the upper 100 m derived from CESM.

2) Within the low-frequency window, both the mesoscale air–sea heat ($\Theta_{\text{temp}}^{\sim 0}$) and momentum ($W_{\text{wind}}^{\sim 0}$) exchange act as eddy killers and play important roles in regulating the energy dissipation. In comparison, $W_{\text{wind}}^{\sim 1}$ is found to drive ageostrophic oceanic processes, while the magnitude of $\Theta_{\text{temp}}^{\sim 1}$ is negligible.

3) The energy budget of EKE_1 is characterized by a balance between $\text{Pres}^{\sim 1}$, $\text{BF}^{\sim 1}$ and $D_K^{\sim 1}$, which can be explained by the TTW theory.

This study has compared the characteristics of mesoscale energy budget and air–sea interaction within the two frequency windows in the KE region. It should be noted that statistical studies based on model output of mixing coefficient (κ and μ) are required to further clarify the detailed processes as to how air–sea interaction can influence the vertical buoyancy fluxes. The evolution of high-frequency processes is not fully analyzed in the present study. Furthermore, recent works have highlighted the role of submesoscale processes in oceanic instability, energy cascade and air–sea interaction (Klein and Lapeyre 2009; McWilliams 2016; Su et al. 2018), but the eddy-resolving model used in this study does not resolve them. How the submesoscale processes modulate the energy balance and air–sea interaction needs to be investigated in detail in the future based on coupled model with higher resolution.

APPENDIX A

Energy Equations

The Navier–Stokes equations under the hydrostatic and Boussinesq approximations are

$$\frac{\partial u}{\partial t} + \nabla \cdot (u\mathbf{v}) - fv = -\frac{1}{\rho_0}\frac{\partial p}{\partial x} + A_{M4}\nabla^4 u + A_{M2}\nabla^2 u + \frac{\partial}{\partial z}\mu\frac{\partial u}{\partial z},$$

(A1)

FIG. B2. Horizontal distribution of (a) $BF_t^{\sim 0}$, (b) $BF_s^{\sim 0}$, (c) $BF_t^{\sim 1}$ and (d) $BF_s^{\sim 1}$ integrated over the upper 200 m. Unit is in $0.01\,\text{W m}^{-2}$, and contours are mean SSH isolines.

$$\frac{\partial v}{\partial t} + \nabla \cdot (v\mathbf{v}) + fu = -\frac{1}{\rho_0}\frac{\partial p}{\partial y} + A_{M4}\nabla^4 v + A_{M2}\nabla^2 v + \frac{\partial}{\partial z}\mu\frac{\partial v}{\partial z},$$
(A2)

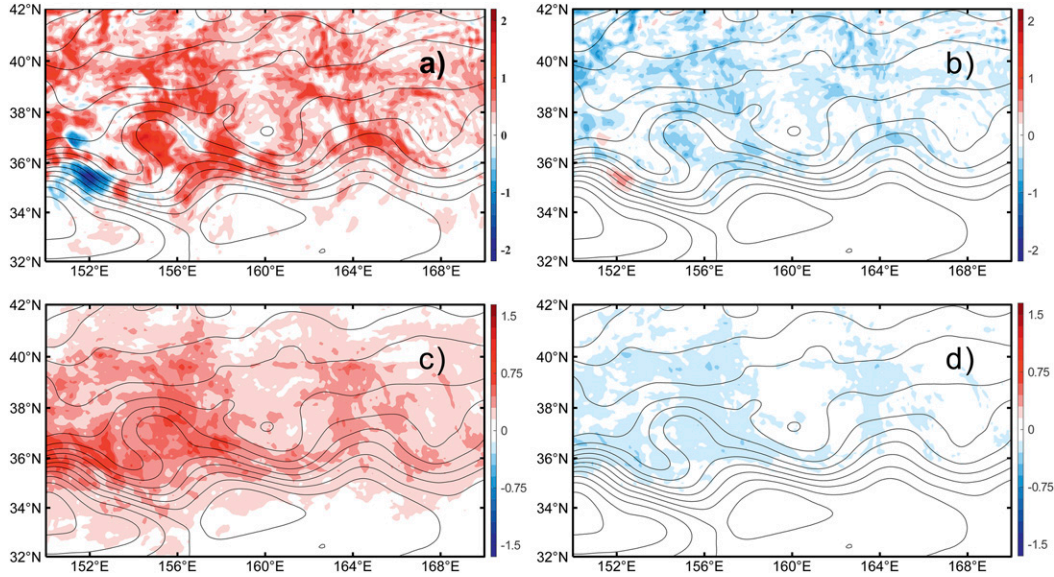$$\nabla \cdot \mathbf{v} = 0,$$
(A3)

$$\frac{\partial p}{\partial z} = -\rho g,$$
(A4)

$$\frac{\partial T^*}{\partial t} + \nabla \cdot (\mathbf{v}T^*) = A_{H4}\nabla^4 T^* + A_{H2}\nabla^2 T^* + \frac{\partial}{\partial z}\kappa\frac{\partial T^*}{\partial z} + F_T,$$
(A5)

Here, T^* presents potential temperature. In the CESM model, the air–sea interaction terms are involved via the sea surface boundary ($z = 0$) conditions (Smith et al. 2010):

$$\mu\frac{\partial \mathbf{u}}{\partial z} = \frac{\tau}{\rho_0},$$
(A6)

$$\kappa\frac{\partial T}{\partial z} = \frac{Q_{\text{net}}}{c_p\rho_0}.$$
(A7)

We first decompose T^* as

$$T^* = T_0(z) + T,$$
(A8)

where $T_0(z)$ denotes the potential temperature averaged over the z plane and time. Substituting Eqs. (A3) and (A8) into Eq. (A5), we obtain

$$\frac{\partial T}{\partial t} + \nabla \cdot (\mathbf{v}T) + w\frac{\partial T_0(z)}{\partial z} = A_{H4}\nabla^4 T + A_{H2}\nabla^2 T + \frac{\partial}{\partial z}\kappa\frac{\partial[T + T_0(z)]}{\partial z} + F_T.$$
(A9)

To obtain the mesoscale energy equations, the variables are decomposed into its mean and mesoscale components:

$$A = \overline{A} + A'.$$
(A10)

Here the mesoscale component is defined as the variability associated with zonally perturbed flows between 150° and 170°E. Sensitivity tests suggest that using different regions (e.g., 145°–165°E) does not substantially affect the result of energetic analysis. It should be noted that this decomposition cannot fully exclude ageostrophic information in the mesoscale component, especially within the high-frequency window. Substituting Eq. (A10) into Eqs. (A1)–(A4) and Eq. (A9), executing the terms that are purely caused by mean flow, we have

$$\frac{\partial u'}{\partial t} + \mathbf{v} \cdot \nabla u' + v' \cdot \nabla \overline{u} - fv' = -\frac{1}{\rho_0}\frac{\partial p'}{\partial x} + A_{M4}\nabla^4 u'$$
$$+ A_{M2}\nabla^2 u' + \frac{\partial}{\partial z}\left(\mu\frac{\partial u}{\partial z}\right)',$$
(A11)

$$\frac{\partial v'}{\partial t} + \mathbf{v} \cdot \nabla v' + v' \cdot \nabla \overline{v} + fu' = -\frac{1}{\rho_0}\frac{\partial p'}{\partial y} + A_{M4}\nabla^4 u'$$
$$+ A_{M2}\nabla^2 v' + \frac{\partial}{\partial z}\left(\mu\frac{\partial v}{\partial z}\right)',$$
(A12)

$$\nabla \cdot v' = 0,$$
(A13)

$$\frac{\partial p'}{\partial z} = -\rho' g,$$
(A14)

$$\frac{\partial T'}{\partial t} + \mathbf{v} \cdot \nabla T' + v' \cdot \nabla \overline{T} + w'\frac{\partial T_0(z)}{\partial z} = A_{H4}\nabla^4 T'$$
$$+ A_{H2}\nabla^2 T' + \frac{\partial}{\partial z}\left\{\kappa\frac{\partial[T + T_0(z)]}{\partial z}\right\}' + F_T'.$$
(A15)

By taking the low-frequency component of Eq. (A14) and multiplying it by $w'^{\sim 0}$, we get

$$\frac{\partial p'^{\sim 0}}{\partial z}w'^{\sim 0} = -p'^{\sim 0}w'^{\sim 0}g. \tag{A16}$$

Using the low-frequency component of Eq. (A13) and combining it with Eq. (A16), we have

$$\frac{\partial(p'^{\sim 0}w'^{\sim 0})}{\partial z} + p'^{\sim 0}\left(\frac{\partial u'^{\sim 0}}{\partial x} + \frac{\partial v'^{\sim 0}}{\partial x}\right) = -p'^{\sim 0}w'^{\sim 0}g. \tag{A17}$$

Multiplying the low-frequency component of Eqs. (A11) and (A12) by $u'^{\sim 0}$ and $v'^{\sim 0}$, respectively, summing them and substituting into Eq. (A17), we obtain Eq. (2a) for the $\mathrm{EKE_0}$ equation. Similarly, by taking the low-frequency component of Eq. (A15) and multiplying by $T'^{\sim 0}$, we have Eq. (2b) for the mesoscale temperature variance equation in the low-frequency window. Considering the complex formats of BT and $\mathrm{BC_{temp}}$, we treat them as residual in the calculation to avoid calculation bias as CESM saves all the terms in Eqs. (A1), (A2), and (A5).

In the surface layer, $(\partial/\partial z)\mu(\partial \mathbf{u}/\partial z)$ associated with wind stress is approximate to constant and surface wind stress is zero at the bottom of this layer. Therefor the friction due to wind forcing in the surface layer can be represented by $\tau/\rho_0 h_1$. Multiplying its mesoscale low-frequency component by $(\rho_0 u'^{\sim 0}, \rho_0 v'^{\sim 0})$ we get $W_{\mathrm{wind}}^{\sim 0}$ in Eq. (3). Using the same method and assumption, we can get $\Theta_{\mathrm{temp}}^{\sim 0}$ in Eq. (4). The equations within the high-frequency window can be derived through the same procedures.

APPENDIX B

Relative Importance of Temperature and Salinity in Regulating EPE

In CESM model, the relationship between density, temperature, and salinity can be approximated as (Smith et al. 2010):

$$\rho'^{\sim 0} = \alpha T'^{\sim 0} + \beta S'^{\sim 0}, \tag{B1a}$$

$$\rho'^{\sim 1} = \alpha T'^{\sim 1} + \beta S'^{\sim 1}, \tag{B1b}$$

where the reference values for α and β are $-0.25\,\mathrm{kg\,m^{-3}\,^{\circ}C^{-1}}$ and $0.76\,\mathrm{kg\,m^{-3}\,(g\,kg^{-1})^{-1}}$, respectively. We have tested the robustness of this approximation and found that it works well in the upper-layer KE region (not shown). Based on this equation, estimating the amplitudes of $(\alpha T'^{\sim 0})^2$ and $(\beta S'^{\sim 0})^2$ $[(\alpha T'^{\sim 1})^2$ and $(\beta S'^{\sim 1})^2]$ provides a direct way to measure their relative importance. Figure B1 compares the horizontal distribution of depth-mean T variance and S variance in the upper 100 m. It is found that amplitude of T variance is more than 3 times larger in both windows, indicating the controlling role of temperature variability in regulating EPE. Besides the comparison of magnitude, the relative importance of temperature and salinity can also be understood in terms of BF term by decomposing it into the temperature-induced and salinity-induced components:

$$\mathrm{BF}^{\sim 0} = \mathrm{BF}_t^{\sim 0} + \mathrm{BF}_s^{\sim 0} = -\alpha T'^{\sim 0}w'^{\sim 0}g - \beta S'^{\sim 0}w'^{\sim 0}g, \tag{B2a}$$

$$\mathrm{BF}^{\sim 1} = \mathrm{BF}_t^{\sim 1} + \mathrm{BF}_s^{\sim 1} = -\alpha T'^{\sim 1}w'^{\sim 1}g - \beta S'^{\sim 1}w'^{\sim 1}g. \tag{B2b}$$

Compared to $\mathrm{BF}_s^{\sim 0}$ $(\mathrm{BF}_s^{\sim 1})$, $\mathrm{BF}_t^{\sim 0}$ $(\mathrm{BF}_t^{\sim 1})$ is also more than 3 times larger (Fig. B2). Therefore, it can be concluded that EPE in the KE region is dominated by variability of temperature, which is consistent with previous estimation (Yang et al. 2019).

REFERENCES

Berloff, P., and J. McWilliams, 1999: Large-scale, low-frequency variability in wind-driven ocean gyres. *J. Phys. Oceanogr.*, **29**, 1925–1949, https://doi.org/10.1175/1520-0485(1999)029<1925:LSLFVI>2.0.CO;2.

Bishop, S. P., 2013: Divergent eddy heat fluxes in the Kuroshio Extension at 144°–148°E. Part II: Spatiotemporal variability. *J. Phys. Oceanogr.*, **43**, 2416–2431, https://doi.org/10.1175/JPO-D-13-061.1.

——, F. Bryan, and R. Small, 2015: Bjerknes-like compensation in the wintertime North Pacific. *J. Phys. Oceanogr.*, **45**, 1339–1355, https://doi.org/10.1175/JPO-D-14-0157.1.

——, R. J. Small, F. O. Bryan, and R. A. Tomas, 2017: Scale dependence of midlatitude air–sea interaction. *J. Climate*, **30**, 8207–8221, https://doi.org/10.1175/JCLI-D-17-0159.1.

Booth, J., L. Thompson, J. Patoux, K. Kelly, and S. Dickinson, 2010: The signature of the midlatitude tropospheric storm tracks in the surface winds. *J. Climate*, **23**, 1160–1174, https://doi.org/10.1175/2009JCLI3064.1.

Chelton, D., M. Schlax, M. Freilich, and R. Milliff, 2004: Satellite measurements reveal persistent small-scale features in ocean winds. *Science*, **303**, 978–983, https://doi.org/10.1126/science.1091901.

Cornillon, P., and K. Park, 2001: Warm core ring velocities inferred from NSCAT. *Geophys. Res. Lett.*, **28**, 575–578, https://doi.org/10.1029/2000GL011487.

Eden, C., and H. Dietze, 2009: Effects of mesoscale eddy/wind interactions on biological new production and eddy kinetic energy. *J. Geophys. Res.*, **114**, C05023, https://doi.org/10.1029/2008JC005129.

Gan, B., and L. Wu, 2015: Feedbacks of sea surface temperature to wintertime storm tracks in the North Atlantic. *J. Climate*, **28**, 306–323, https://doi.org/10.1175/JCLI-D-13-00719.1.

Gaube, P., D. Chelton, R. Samelson, M. Schlax, and L. O'Neill, 2015: Satellite observations of mesoscale eddy-induced Ekman pumping. *J. Phys. Oceanogr.*, **45**, 104–132, https://doi.org/10.1175/JPO-D-14-0032.1.

Gula, J., M. Molemaker, and J. McWilliams, 2014: Submesoscale cold filaments in the Gulf Stream. *J. Phys. Oceanogr.*, **44**, 2617–2643, https://doi.org/10.1175/JPO-D-14-0029.1.

Jing, Z., P. Chang, X. Shan, S. Wang, L. Wu, and J. Kurian, 2019: Mesoscale SST dynamics in the Kuroshio–Oyashio extension region. *J. Phys. Oceanogr.*, **49**, 1339–1352, https://doi.org/10.1175/JPO-D-18-0159.1.

——, and Coauthors, 2020: Maintenance of mid-latitude oceanic fronts by mesoscale eddies. *Sci. Adv.*, **6**, eaba7880, https://doi.org/10.1126/sciadv.aba7880.

Kelly, K., S. Dickinson, M. McPhaden, and G. Johnson, 2001: Ocean currents evident in satellite wind data. *Geophys. Res. Lett.*, **28**, 2469–2472, https://doi.org/10.1029/2000GL012610.

——, R. Small, R. Samelson, B. Qiu, T. Joyce, Y. Kwon, and M. Cronin, 2010: Western boundary currents and frontal air–sea interaction: Gulf Stream and Kuroshio Extension. *J. Climate*, **23**, 5644–5667, https://doi.org/10.1175/2010JCLI3346.1.

Kida, S., and Coauthors, 2015: Oceanic fronts and jets around Japan: A review. *J. Oceanogr.*, **71**, 469–497, https://doi.org/10.1007/s10872-015-0283-7.

Klein, P., and G. Lapeyre, 2009: The oceanic vertical pump induced by mesoscale and submesoscale turbulence. *Annu. Rev. Mar. Sci.*, **1**, 351–375, https://doi.org/10.1146/annurev.marine.010908.163704.

Konda, M., H. Ichikawa, H. Tomita, and M. Cronin, 2010: Surface heat flux variations across the Kuroshio Extension as observed by surface flux buoys. *J. Climate*, **23**, 5206–5221, https://doi.org/10.1175/2010JCLI3391.1.

Large, W., and S. Yeager, 2009: The global climatology of an interannually varying air-sea flux data set. *Climate Dyn.*, **33**, 341–364, https://doi.org/10.1007/s00382-008-0441-3.

——, J. McWilliams, and S. Doney, 1994: Oceanic vertical mixing—A review and a model with a nonlocal boundary-layer parameterization. *Rev. Geophys.*, **32**, 363–403, https://doi.org/10.1029/94RG01872.

Liang, X. S., 2016: Canonical transfer and multiscale energetics for primitive and quasigeostrophic atmospheres. *J. Atmos. Sci.*, **73**, 4439–4468, https://doi.org/10.1175/JAS-D-16-0131.1.

——, and A. Robinson, 2005: Localized multiscale energy and vorticity analysis: I. Fundamentals. *Dyn. Atmos. Oceans*, **38**, 195–230, https://doi.org/10.1016/j.dynatmoce.2004.12.004.

Liu, X., P. Chang, J. Kurian, R. Saravanan, and X. Lin, 2018: Satellite observed precipitation response to ocean mesoscale eddies. *J. Climate*, **31**, 6879–6895, https://doi.org/10.1175/JCLI-D-17-0668.1.

Lorenz, E., 1955: Available potential energy and the maintenance of the general circulation. *Tellus*, **7**, 157–167, https://doi.org/10.3402/tellusa.v7i2.8796.

Ma, X., and Coauthors, 2016: Western boundary currents regulated by interaction between ocean eddies and the atmosphere. *Nature*, **535**, 533–537, https://doi.org/10.1038/nature18640.

McWilliams, J., 2016: Submesoscale currents in the ocean. *Proc. Roy. Soc.*, **472A**, 20160117, https://doi.org/10.1098/rspa.2016.0117.

Nakamura, H., T. Sampe, Y. Tanimoto, and A. Shimpo, 2004: Observed associations among storm tracks, jet streams and midlatitude oceanic fronts. *Earth's Climate: The Ocean–Atmosphere Interaction, Geophys. Monogr.*, Vol. 147, Amer. Geophys. Union, 329–346.

Nakano, H., H. Tsujino, and K. Sakamoto, 2013: Tracer transport in cold-core rings pinched off from the Kuroshio Extension in an eddy-resolving ocean general circulation model. *J. Geophys. Res. Oceans*, **118**, 5461–5488, https://doi.org/10.1002/jgrc.20375.

Qiu, B., 2001: Kuroshio and Oyashio currents. *Encyclopedia of Ocean Sciences*, Academic Press, 1413–1425.

——, and S. Chen, 2005: Variability of the Kuroshio Extension jet, recirculation gyre, and mesoscale eddies on decadal time scales. *J. Phys. Oceanogr.*, **35**, 2090–2103, https://doi.org/10.1175/JPO2807.1.

——, and ——, 2010: Eddy-mean flow interaction in the decadally modulating Kuroshio Extension system. *Deep-Sea Res. II*, **57**, 1098–1110, https://doi.org/10.1016/j.dsr2.2008.11.036.

——, and ——, 2011: Effect of decadal Kuroshio Extension jet and eddy variability on the modification of North Pacific Intermediate Water. *J. Phys. Oceanogr.*, **41**, 503–515, https://doi.org/10.1175/2010JPO4575.1.

——, K. Kelly, and T. Joyce, 1991: Mean flow and variability in the Kuroshio Extension from Geosat altimetry data. *J. Geophys. Res.*, **96**, 18 491–18 507, https://doi.org/10.1029/91JC01834.

——, S. Chen, N. Schneider, and B. Taguchi, 2014: A coupled decadal prediction of the dynamic state of the Kuroshio Extension system. *J. Climate*, **27**, 1751–1764, https://doi.org/10.1175/JCLI-D-13-00318.1.

——, ——, and ——, 2017: Dynamical links between the decadal variability of the Oyashio and Kuroshio Extensions. *J. Climate*, **30**, 9591–9605, https://doi.org/10.1175/JCLI-D-17-0397.1.

Renault, L., M. J. Molemaker, J. C. McWilliams, A. F. Shchepetkin, F. Lemarié, D. Chelton, S. Illig, and A. Hall, 2016: Modulation of wind work by oceanic current interaction with the atmosphere. *J. Phys. Oceanogr.*, **46**, 1685–1704, https://doi.org/10.1175/JPO-D-15-0232.1.

——, J. McWilliams, and S. Masson, 2017: Satellite observations of imprint of oceanic current on wind stress by air-sea coupling. *Sci. Rep.*, **7**, 17747, https://doi.org/10.1038/s41598-017-17939-1.

Reynolds, W., T. Smith, C. Liu, D. Chelton, K. Casey, and M. Schlax, 2007: Daily high-resolution-blended analyses for sea surface temperature. *J. Climate*, **20**, 5473–5496, https://doi.org/10.1175/2007JCLI1824.1.

Sampe, T., and S.-P. Xie, 2007: Mapping high sea winds from space: A global climatology. *Bull. Amer. Meteor. Soc.*, **88**, 1965–1978, https://doi.org/10.1175/BAMS-88-12-1965.

Sasaki, Y., and S. Minobe, 2015: Climatological mean features and interannual to decadal variability of ring formations in the Kuroshio Extension region. *J. Oceanogr.*, **71**, 499–509, https://doi.org/10.1007/s10872-014-0270-4.

Seo, H., A. Miller, and J. Norris, 2016: Eddy–wind interaction in the California Current System: Dynamics and impacts. *J. Phys. Oceanogr.*, **46**, 439–459, https://doi.org/10.1175/JPO-D-15-0086.1.

Shan, X., Z. Jing, B. Gan, L. Wu, P. Chang, X. Ma, S. Wang, Z. Chen, and H. Yang, 2020: Surface heat flux induced by mesoscale eddies cools the Kuroshio-Oyashio Extension region. *Geophys. Res. Lett.*, **47**, e2019GL086050, https://doi.org/10.1029/2019GL086050.

Small, R., and Coauthors, 2008: Air–sea interaction over ocean fronts and eddies. *Dyn. Atmos. Oceans*, **45**, 274–319, https://doi.org/10.1016/j.dynatmoce.2008.01.001.

——, and Coauthors, 2014: A new synoptic scale resolving global climate simulation using the Community Earth System Model. *J. Adv. Model. Earth Syst.*, **6**, 1065–1094, https://doi.org/10.1002/2014MS000363.

Smith, R., and Coauthors, 2010: The Parallel Ocean Program (POP) reference manual. Ocean Component of the Community Climate System Model (CCSM), 141 pp., https://www.cesm.ucar.edu/models/cesm1.1/pop2/doc/sci/POPRefManual.pdf.

Su, Z., J. Wang, P. Klein, A. F. Thompson, and D. Menemenlis, 2018: Ocean submesoscales as a key component of the global heat budget. *Nat. Commun.*, **9**, 775, https://doi.org/10.1038/s41467-018-02983-w.

Taguchi, B., S. Xie, N. Schneider, M. Nonaka, H. Sasaki, and Y. Sasai, 2007: Decadal variability of the Kuroshio Extension: Observations and an eddy-resolving model hindcast. *J. Climate*, **20**, 2357–2377, https://doi.org/10.1175/JCLI4142.1.

Taylor, J., and R. Ferrari, 2010: Buoyancy and wind-driven convection at mixed layer density fronts. *J. Phys. Oceanogr.*, **40**, 1222–1242, https://doi.org/10.1175/2010JPO4365.1.

Waterman, S., and S. Jayne, 2011: Eddy–mean flow interaction in the along-stream development of a western boundary current jet: An idealized model study. *J. Phys. Oceanogr.*, **41**, 682–707, https://doi.org/10.1175/2010JPO4477.1.

Xu, C., X. Zhai, and X. Shang, 2016: Work done by atmospheric winds on mesoscale ocean eddies. *Geophys. Res. Lett.*, **43**, 12 174–12 180, https://doi.org/10.1002/2016GL071275.

Yang, H., B. Qiu, P. Chang, L. Wu, S. Wang, Z. Chen, and Y. Yang, 2018: Decadal variability of eddy characteristics and energetics in the Kuroshio Extension: Unstable versus stable states. *J. Geophys. Res. Oceans*, **123**, 6653–6669, https://doi.org/10.1029/2018JC014081.

——, P. Chang, B. Qiu, Q. Zhang, L. Wu, Z. Chen, and H. Wang, 2019: Mesoscale air–sea interaction and its role in eddy energy dissipation in the Kuroshio Extension. *J. Climate*, **32**, 8659–8676, https://doi.org/10.1175/JCLI-D-19-0155.1.

Yang, Y., and X. Liang, 2016: The instabilities and multiscale energetics underlying the mean–interannual–eddy interactions in the Kuroshio Extension region. *J. Phys. Oceanogr.*, **46**, 1477–1494, https://doi.org/10.1175/JPO-D-15-0226.1.

——, and ——, 2018: On the seasonal eddy variability in the Kuroshio Extension. *J. Phys. Oceanogr.*, **48**, 1675–1689, https://doi.org/10.1175/JPO-D-18-0058.1.

——, ——, B. Qiu, and S. Chen, 2017: On the decadal variability of the eddy kinetic energy in the Kuroshio Extension. *J. Phys. Oceanogr.*, **47**, 1169–1187, https://doi.org/10.1175/JPO-D-16-0201.1.

Yasuda, I., 2003: Hydrographic structure and variability in the Kuroshio–Oyashio transition area. *J. Oceanogr.*, **59**, 389–402, https://doi.org/10.1023/A:1025580313836.